ACS APPLIED MATERIALS & INTERFACES
Research Article
www.acsami.org

Recrystallization of Highly-Mismatched $Be_xZn_{1-x}O$ Alloys: Formation of a Degenerate Interface

Dae-Sung Park,[†] Sepehr K. Vasheghani Farahani,[†] Marc Walker,[†] James J. Mudd,[†] Haiyuan Wang,[†] Aleksander Krupski,[†] Einar B. Thorsteinsson,[‡] Djelloul Seghier,[‡] Chel-Jong Choi,[¶] Chang-Ju Youn,[¶] and Chris F. McConville*,[†]

[†]Department of Physics, University of Warwick, Coventry CV4 7AL, United Kingdom

[‡]Science Institute, University of Iceland, Dunhaga 3, Reykjavik IS-107, Iceland

[¶]School of Semiconductor and Chemical Engineering, Semiconductor Physics Research Center (SPRC), Chonbuk National University, Jeonju, North Jeolla 561-756, Republic of Korea

Supporting Information

ABSTRACT: We investigate the effect of thermally induced phase transformations on a metastable oxide alloy film, a multiphase $Be_xZn_{1-x}O$ (BZO), grown on $Al_2O_3(0001)$ substrate for annealing temperatures in the range of 600–950 °C. A pronounced structural transition is shown together with strain relaxation and atomic redistribution in the annealed films. Increasing annealing temperature initiates out-diffusion and segregation of Be and subsequent nucleation of nanoparticles at the surface, corresponding to a monotonic decrease in the lattice phonon energies and band gap energy of the films. Infrared reflectance simulations identify a highly conductive ZnO interface layer (thicknesses in the range of ≈10–29 nm for annealing temperatures ≥800 °C). The highly degenerate interface layers with temperature-independent carrier concentration and mobility significantly influence the electronic and optical properties of the BZO films. A parallel conduction model is employed to determine the carrier concentration and conductivity of the bulk and interface regions. The density-of-states-averaged effective mass of the conduction electrons for the interfaces is calculated to be in the range of $0.31m_0$ and $0.67m_0$. A conductivity as high as 1.4×10^3 S·cm^{-1} is attained, corresponding to the carrier concentration $n_{Int} = 2.16 \times 10^{20}$ cm^{-3} at the interface layers, and comparable to the highest conductivities achieved in highly doped ZnO. The origin of such a nanoscale degenerate interface layer is attributed to the counter-diffusion of Be and Zn, rendering a high accumulation of Zn interstitials and a giant reduction of charge-compensating defects. These observations provide a broad understanding of the thermodynamics and phase transformations in $Be_xZn_{1-x}O$ alloys for the application of highly conductive and transparent oxide-based devices and fabrication of their alloy nanostructures.

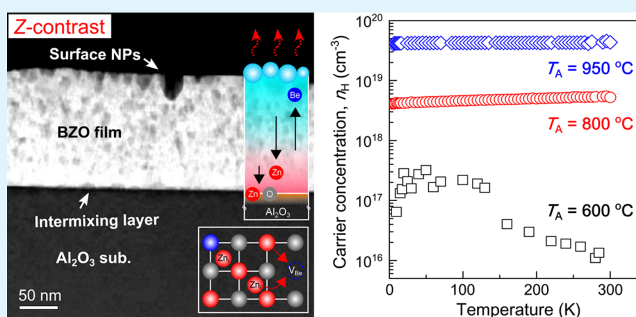

KEYWORDS: *phase transformation, oxide alloys, BeZnO, degenerate interface, atomic diffusion, defect engineering*

1. INTRODUCTION

Recent progress in the advancement of oxide-based optoelectronics has been accomplished through improved control of oxide film growth and allowing the fabrication of artificial heterostructures,[1,2] the effective control of ionic polarity and intentional/unintentional doping,[3−5] and band gap engineering of these materials.[6−8] The surface and interface regions of oxides give rise to exotic and interesting physical and chemical phenomena such as band bending, Fermi-level pinning, surface reconstruction, and highly accumulated charge carriers at oxide heterointerfaces.[9−12] These are primarily associated with the distribution of a number of neutral or charged point defects/impurities, the removal of surface atoms, and structural defects such as threading dislocations or planar defects/grain boundaries.

Wide direct band gap zinc oxide (ZnO)-based materials have promising properties such as: large exciton binding energy (≈60 meV); unintentional *n*-type conductivity; high transparency in the near-ultraviolet and visible ranges; and the high natural abundance.[13,14] These materials provide opportunities for the fabrication of optoelectronic devices, e.g., laser diodes (LDs), light emitting diodes (LEDs), high electron mobility transistors (HEMTs), UV sensors, and their nanoscale structures in device applications.[1,15−18] However, there are persistent issues in ZnO materials including: difficulties of *p*-type doping due to unintentional/extrinsic *n*-type hydrogen impurities[5] and the position of the charge neutrality level

Received: July 5, 2014
Accepted: October 7, 2014
Published: October 7, 2014

© 2014 American Chemical Society

(CNL), i.e., the energy at which defect states change from donor-type to acceptor-type with reference to the Fermi level, being above the conduction band minimum;[19] thermal instability at high temperature (above 600 °C); and the distribution of thermally created defects such as interstitial Zn (Zn_i), Zn vacancy (V_{Zn}), interstitial oxygen (O_i), and oxygen vacancy (V_O).[20,21] The formation of such intrinsic defects, which create states in the band gap of ZnO, strongly depends on the experimental conditions, namely, thermodynamic equilibrium.

Band gap engineering of ZnO is profoundly important to the design of quantum structures in respect to electron confinement for the enhancement of optoelectronic performance.[1,22] Limitations of band gap modulation for $Mg_xZn_{1-x}O$ (Mg fraction: $x \leq 0.33$) and $Cd_xZn_{1-x}O$ alloys (Cd fraction: $x \leq 0.07-0.69$) have been reported due to the structural difference between hexagonal ZnO and cubic MgO/CdO.[6,23] As a result, $Be_xZn_{1-x}O$ ternary alloys have been considered as an alternative since both ZnO and BeO possess wurtzite (WZ) crystal structures.[22] However, structural fluctuation, e.g., phase separation, occurs due to large differences in atomic size between Zn (3.06 Å) and Be (2.80 Å) and their large chemical difference;[24] differences in formation enthalpies;[25] and substantial strain caused by highly mismatched underlying substrates, e.g., Si and Al_2O_3.[26−28] The phase stabilization of $Be_xZn_{1-x}O$ alloys is the subject of experimental and theoretical studies to date aiming to achieve homogeneous $Be_xZn_{1-x}O$ alloys. Hence, understanding the thermodynamics of Be and following phase transitions in the alloy system is essential to control solid-state reactions and the resulting physical and chemical properties.

In the present study, we explore the effect of thermal treatment on an inhomogeneous $Be_xZn_{1-x}O$ (BZO) film grown on $Al_2O_3(0001)$ at annealing temperatures up to 950 °C. Thermal annealing induces significant recrystallization via strain relaxation and atomic redistribution of the multiphase crystalline films. This results in considerable microsegregation of BeO and ZnO phases within the film combined with the formation of a crystalline ZnO interface layer. X-ray photoelectron spectroscopy (XPS) along with infrared (IR) reflectance measurements and simulations clearly show the out-diffusion of Be atoms and precipitation of lattice point defects in the BZO films with increasing annealing temperature (T_A). Highly conductive layers emerge at the BZO/Al_2O_3 interface for $T_A \geq 800$ °C. As a consequence, carrier concentration, conductivity, and density-of-state averaged effective masses of the degenerate interfaces are separately determined by applying a two-layer model for the high-temperature annealed BZO films. High accumulation of Be (Zn) at the surface (interface) is addressed by the migration of cations during high-temperature annealing based on a counter-diffusion mechanism to elucidate the formation of the highly degenerate interface layer in the alloy film.

2. RESULTS AND DISCUSSION

2.1. Recrystallization and Atomic Distribution in BZO Films. Significant recrystallization of the as-grown multiphase BZO film on an $Al_2O_3(0001)$ substrate was observed, showing a visible structural transition at $T_A \geq 700$ °C [see Figures S1 and S2 in the Supporting Information]. The Be composition of ≈6% of the as-grown alloy film was determined from XRD measurements by using Vegard's law.[29] The phase separation and structural fluctuation in the multiphase alloy film were interpreted by changes in the local composition of Be caused by thermal instability and lattice strain in this highly mismatched heterostructure.[24,28] Therefore, we attribute the recrystallization of the multiphase crystalline film to the redistribution of Be and strain relaxation following annealing.

Transmission electron microscopy (TEM) measurements were performed in order to understand the microstructural properties of the recrystallized BZO film at T_A = 950 °C. Figure 1a shows cross-sectional TEM images of an annealed BZO film.

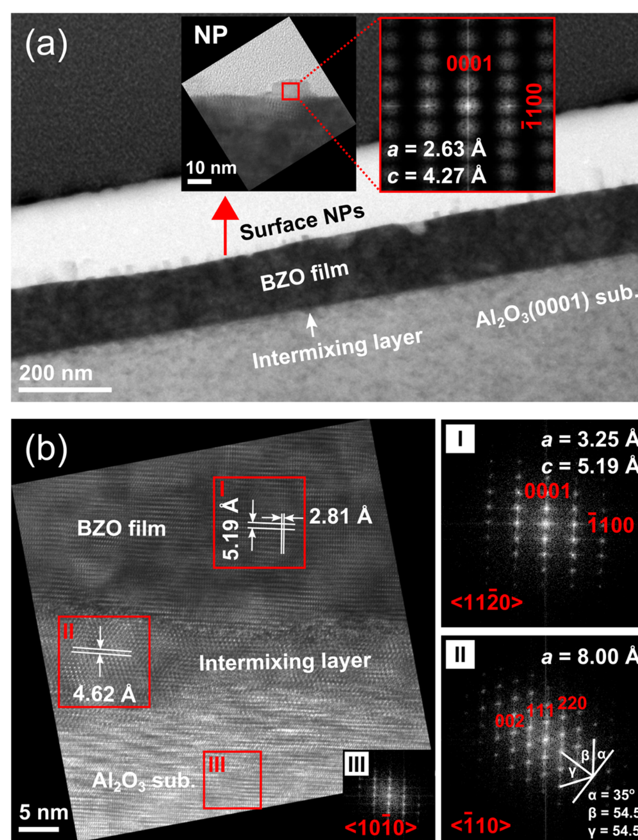

Figure 1. (a) Cross-sectional TEM image of the annealed BZO film on an $Al_2O_3(0001)$ substrate (T_A = 950 °C). The annealed film is formed of (i) surface nanoparticles (NPs) [the top inset], (ii) the main film, and (iii) the intermixing layer. The insets are high resolution TEM images of the NP and Fast-Fourier transform (FFT) associated with the red-square area in the HRTEM image. (b) HRTEM image along the <112̄0>-zone axis of the BZO/Al_2O_3 interface region. The selected red-squares I, II, and III represent the main film, intermixing layer, and substrate, respectively. The corresponding FFTs of the red-square areas I and II indicate WZ and face-centered cubic (FCC) structures. The extracted lattice constants are shown in the images I and II.

The total thickness of the film was found to be 152 ± 8 nm. The recrystallized film consists of three distinct regions: (i) nanoparticles (NPs) at the surface [the top inset], (ii) the main film, and (iii) the intermixing layer. The crystallization of the NPs is WZ phase BeO with the calculated lattice constants, a = 2.63 Å and c = 4.27 Å.[30] The T_A dependent size and distribution of the nanodroplets/NPs at the surface of the annealed films were also observed in AFM (Figure S3 in the Supporting Information). A detailed mechanism for the formation and behavior of the NPs at the surface of the annealed BZO films has been presented in our previous study.[30]

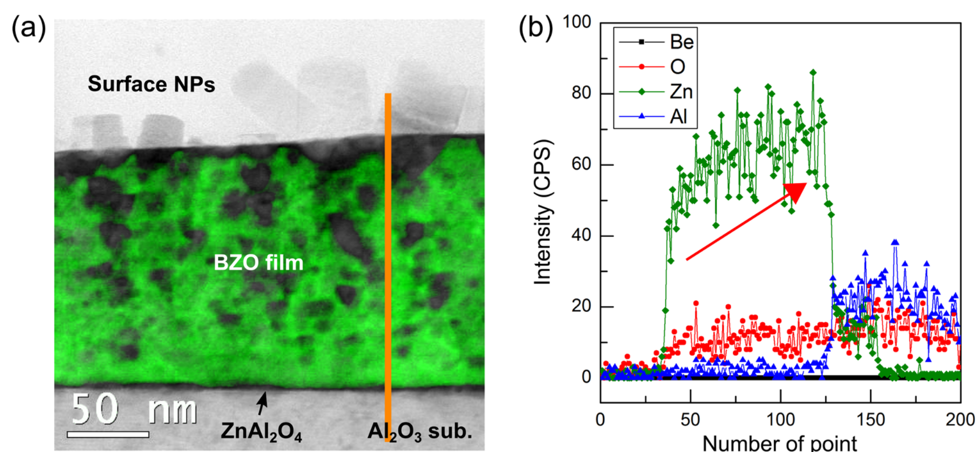

Figure 2. (a) Cross-sectional STEM image of the BZO film annealed at T_A = 950 °C. The image is presented by merging bright-field (gray) and annular dark-field (green) images. (b) Energy dispersive X-ray spectroscopy (EDS) line scan across the annealed BZO film. The EDS line profiles for the composed elements (Be, O, Zn, and Al) across the sample correspond to the orange vertical solid line in (a).

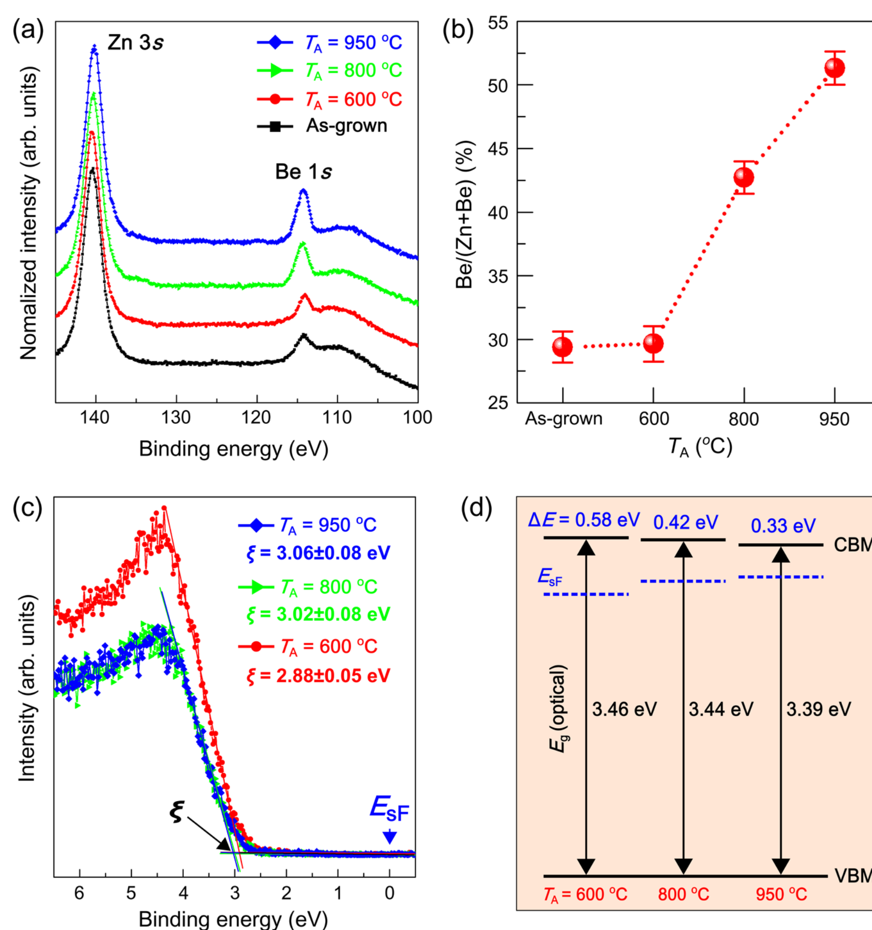

Figure 3. (a) Normalized XPS spectra of Zn 3s and Be 1s core-levels. (b) The relative ratio (%) of surface Be concentration to Zn [Be/(Zn + Be)] for the as-grown and annealed BZO films (T_A = 600, 800, and 950 °C). (c) Valence band (VB) photoemission spectra for the surface of the annealed films. The values of ξ indicate the separation of the VB maximum and surface Fermi level (E_{sF}). (d) A diagram of E_{sF} under a change of the band gap energy for the BZO films annealed at T_A = 600, 800, and 950 °C. The values of ΔE denote the separation of the optical band gap (E_g) to E_{sF} for the annealed films.

Figure 1b shows the high resolution transmission electron microscopy (HRTEM) image along the <11$\bar{2}$0>-zone axis for the interface region of the annealed film at T_A = 950 °C. The structural properties of the three different regions, namely, BZO film, intermixing layer, and substrate were examined separately by selecting the red-square areas I, II, and III, respectively. The associated Fast-Fourier transform (FFT) of the red-square I shows typical spots representative of WZ structure. The lattice constants of the film were determined to be a = 3.25 Å and c = 5.19 Å by extracting the plane spacing of

0001 and $\bar{1}100$. These are almost identical to that of bulk ZnO (a = 3.25 Å and c = 5.20 Å) [see the upper-right FFT image I in Figure 1b].[31] This is indicative of a low Be composition or even no Be in the annealed BZO film (T_A = 950 °C) near the BZO/Al_2O_3 interface.

Crystallization of a new interfacial layer (≤10 nm thick) was found at the BZO/Al_2O_3 interface region as denoted by the red-square II of Figure 1b. The corresponding FFT pattern displays a face centered cubic (FCC) structure with interaxial angles between the planes as shown in the bottom-right image II of Figure 1b. The obtained lattice constant, a = 8.00 Å, is close to that of $ZnAl_2O_4$, a = 8.086 Å.[32,33] Hence, the formation of the layer is believed to be caused by an interfacial solid-state reaction of ZnO and Al_2O_3 at high annealing temperatures. This results in the crystallization of spinel $ZnAl_2O_4$ or Zn-deficient phase $Zn_xAl_yO_z$ at the interface depending on the degree of the atomic diffusion of Zn and O into Al_2O_3, i.e., $(ZnO)_n + (Al_2O_3)_m$. Furthermore, the orientation relationship between the annealed BZO film, thermally crystallized $ZnAl_2O_4$, and Al_2O_3 were determined to be present with $[0001]_{BZO} \| [111]_{ZnAl_2O_4} \| [0001]_{Al_2O_3}$ and $[10\bar{1}0]_{BZO} \| [\bar{1}\bar{1}2]_{ZnAl_2O_4} \| [11\bar{2}0]_{Al_2O_3}$.

Figure 2a displays a cross-sectional scanning transmission electron microscopy (STEM) image of the annealed BZO film (T_A = 950 °C). The STEM image is created by merging the bright-field (phase contrast in gray color) and annular dark-field (Z-contrast in green color) images to obtain clear visualization of the spatial distribution of elements. The contrast in the bright field image is correlated to the mass−thickness and diffraction, while the intensity, I, of the Z-contrast dark field imaging by elastically scattered incoherent electrons is proportional to atomic number, Z, according to $I \approx Z^{\alpha}$, where α is a parameter ($\alpha \leq 2$).[34] Hence, the STEM image enables the examination of atomic distribution and chemical composition in the main film and intermixing layer. The vivid contrast between the surface and near interface region was observed in the image [Figure 2a]. This is due to a higher accumulation of lighter Be atoms (larger Zn atoms) at the surface (interface) relative to Zn (Be). Moreover, the density of partially distributed darker spots in the dark field image increases toward the surface of the film, implying an increase in the number of Be and/or BeO clusters closer to the surface. The intensity for the interfacial layer (based on the bright-field STEM) is darker than that of the substrate region (Al_2O_3) which is caused by the intermixing of ZnO and Al_2O_3 and the resulting spinel $ZnAl_2O_4$ or $Zn_xAl_yO_z$ as mentioned earlier.

To further resolve the chemical compositions in the sample, energy dispersive X-ray spectroscopy (EDS) measurements were performed as shown in Figure 2b. The EDS line profiles for each element (Be, O, Zn, and Al) across the specimen correspond to the orange vertical line in Figure 2a. Note that the signal intensity of Be and light atoms is generally underestimated in EDS as the detector is equipped with a Be window.[35] Apart from the limits of the concentration analysis for lighter elements in the sample within the EDS characteristics, an upward gradient in the intensity of Zn was clearly found moving toward the interface, denoted by the red arrow in Figure 2b. This is indicative of an increase in the atomic concentration of Zn toward the interface, which corroborates the locally brighter region in the film close to the interface, relative to the surface and substrate areas, in the Z-contrast STEM image [Figure 2a]. The atomic intermixing of Zn, Al, and O as a result of ZnO diffusion to the top surface of Al_2O_3 substrate was also verified from the EDS profiles of the interface region.

2.2. Surface Chemical Composition and VB Photoemission. Monochromatic XPS measurements were performed to investigate the variation of Be composition and electronic structure as a function of T_A for the surface of the BZO films. Figure 3a shows the normalized XPS spectra of Zn 3s and Be 1s core-levels for the as-grown and annealed BZO films at T_A = 600, 800, and 950 °C. The Be 1s peak located at a BE of 114.25 ± 0.15 eV is attributed to a chemical bonding of the Be−O state (metallic Be states, BE ≈ 111 eV).[24] This results from the incorporation of Be atoms at Zn sites forming a $Be_xZn_{1-x}O$ alloy for the as-grown film. Moreover, the Be 1s peak intensity gradually increased with respect to Zn 3s with increasing T_A, suggesting segregation of Be to the surface and the subsequent formation of BeO phases as observed in the TEM results. By comparing the relative XPS core-level intensities of Zn 3s and Be 1s, it was also observed that the Be composition to Zn (Be/(Zn + Be)) at the surfaces of the ternary films was increased from 29.4% to 51.3% with increasing T_A, up to 950 °C, as shown in Figure 3b. This Be enrichment could be caused by two factors during the thermal treatment process: (i) atomic replacement of interstitially distributed Be atoms onto Zn sites and (ii) out-diffusion of Be atoms toward the surface region.

Utilizing the optical measurements of the BZO films, the absorption edges were obtained by extrapolation of the linear portion to horizontal background of the absorption coefficient (α^2) spectra (shown elsewhere).[30] These results show a continuous decrease of the optical band gap energy with increasing T_A as illustrated in Figure 3d. Therefore, it is believed that the increased Be composition at the film surface is primarily associated with thermally induced out-diffusion of Be atoms. This also supports the surface segregation of Be and the droplet/NP formation, which was observed in the TEM and AFM results.

Figure 3c displays the XPS spectra of valence band (VB) photoemission as a function of T_A for the BZO films. The position of the surface Fermi level (E_{sF}) in the films was determined by extrapolating a linear fit to the sharp edge of the VB spectra. Since the external electrons supplied by a charge neutralizer cause a shift in the near VB region, E_{sF} of the as-grown film is discounted. These data indicate that the VB edges of the BZO films shifted toward the higher BE regions with respect to E_{sF} as T_A increased, corresponding to an upward shift of E_{sF}. Considering the band gap energy (E_g) change from 3.46 eV at T_A = 600 °C to 3.39 eV at T_A = 950 °C, E_{sF} for the BZO films moves toward the conduction band minimum (CBM) as ΔE ($E_g - E_{sF}$) decreases [Figure 3d]. This is suggestive of thermally induced excess donors near the surface together with the reduction of the band gap energy in the films as T_A is increased.

2.3. IR Reflectance Measurement and Simulation Models. IR reflectance measurements were carried out to determine the film thicknesses, IR-active BZO phonon modes, and electron plasma frequencies (assigned to free carrier excitations). According to an irreducible representation of lattice vibration modes for WZ BZO (space group: C_{6v}^4) at the center (Γ-point) of the Brillouin zone, IR active A_1 and E_1 phonon branches are polarized along the z-direction and xy-plane, respectively.[36,37] Both branches are composed of pronounced transverse optical (TO) and longitudinal optical

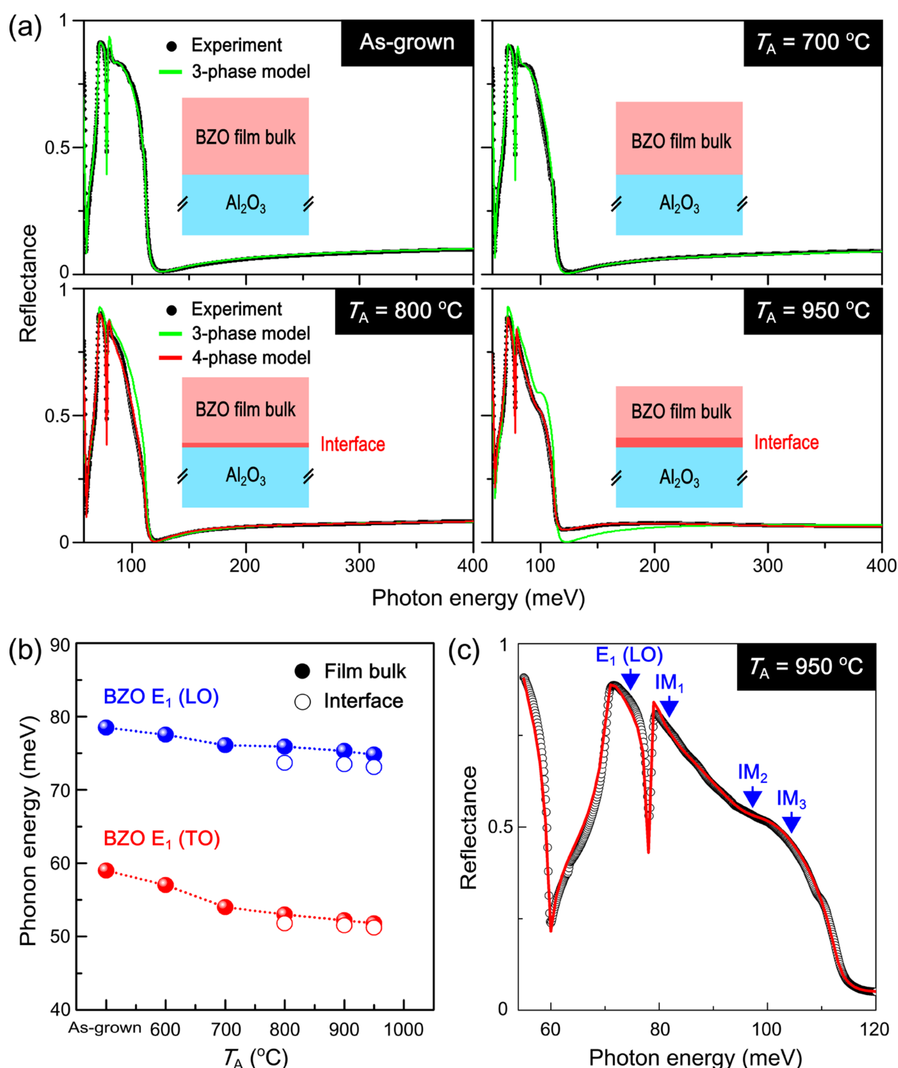

Figure 4. (a) Experimental IR reflectivity spectra (black circle) plotted with the simulated spectra (green and red solid lines). The insets represent schematic diagrams of three-phase model for the as-grown, and 700 °C, and four-phase model for T_A = 800 and 950 °C. (b) Variation of the phonon mode frequencies, E_1(TO) and (LO), of the BZO film bulk (closed circle) and interface (open circle) layers as a function of T_A. (c) Three impurity modes of the BZO films annealed at T_A = 950 °C.

(LO) phonon modes, due to the macroscopic electric field associated with the LO phonons in WZ structure.[38,39] On the basis of the above anisotropic dielectric response of the BZO films, *s*-polarized light has been used to attain $E \perp c$, where E is the electric field of incident light, obtained parallel to the surface. The *s*-polarized reflectance spectra of the BZO films (the as-grown and annealed, T_A = 600 °C) were simulated using the classical Drude model (ϵ_D) for carrier response and the modified expression, which involves the factorized model (ϵ_L) for the host lattice response and a model function (ϵ_{IM}) describing IR-active impurity,[38]

$$\begin{aligned}\epsilon &= (\epsilon_{L,i} + \epsilon_D) \times \epsilon_{IM,j} \\ &= \epsilon(\infty)\left(\prod_i \frac{\omega^2 + i\omega\gamma_{LO,i} - \omega_{LO,i}{}^2}{\omega^2 + i\omega\gamma_{TO,i} - \omega_{TO,i}{}^2} - \frac{\omega_p{}^2}{\omega(\omega + i\gamma_p)}\right) \\ &\times \prod_j \left(1 + \frac{i\omega\delta\gamma_{\nu,j} - \delta\omega_{\nu,j}{}^2}{\omega^2 + i\omega\gamma_{IM,\nu,j} - \omega_{IM,\nu,j}{}^2}\right)\end{aligned} \tag{1}$$

where $\epsilon(\infty)$, ω, $\omega(TO,i)$, $\omega(LO,i)$, $\gamma(TO,i)$, and $\gamma(LO,i)$ are the high frequency dielectric constant, frequency of the incident radiation, frequencies and damping factors of the *i*th TO and LO phonons, respectively. ω_p and γ_p are the resonance plasma frequency and broadening parameter, respectively. $\omega(IM_j)$, $\gamma(IM_j)$, $\delta(IM_j)$, and $\delta\gamma(IM_j)$ are denoted as the frequency and broadening parameter of impurity modes and the LO-TO splitting value and broadening parameter. Additionally, the annealed BZO films at $T_A \geq$ 700 °C indicate high conductivities by room-temperature (RT) Hall effect measurements. The LO-phonon-plasmon (LPP) coupling effect was considered when ω_p was in the range of or close to the LO modes. This was implemented using the factorized LPP model,

$$\begin{aligned}\epsilon &= \epsilon_i^{LPP} \times \epsilon_{IM,j} \\ &= \frac{\epsilon_i^{LPP}(\infty)\prod_i^2 (\omega^2 + i\omega\tilde{\gamma}_{LPP,i} - \tilde{\omega}_{LPP,i}{}^2)}{\omega\prod_i(\omega + i\gamma_p)\prod_i(\omega^2 + i\omega\gamma_{TO,i} - \omega_{TO,i}{}^2)} \times \epsilon_{IM,j}\end{aligned} \tag{2}$$

Table 1. Best-Fit Parameters Used in the IR Simulations for the BZO Films, where T_A, ϵ (∞), E_1 (TO), E_1 (LO), ω_p, and d are Annealing Temperature, High Frequency Dielectric Constant, E_1 Transverse Optical Phonon Frequency, E_1 Longitudinal Optical Phonon Frequency, the Plasma Frequency, and Layer Thickness, Respectively

T_A (°C)	BZO sample	ϵ (∞)	E_1 (TO) (meV)	E_1 (LO) (meV)	ω_p (meV)	d (nm)
as-grown	film layer	3.55 ± 0.05	59.2 ± 0.5	78.5 ± 0.04		212 ± 8
600	film layer	3.55 ± 0.05	57.0 ± 0.3	77.5 ± 0.05	16 ± 12	209 ± 6
700	film layer	3.62 ± 0.02	54.3 ± 0.1	76.1 ± 0.05	42 ± 8	208 ± 8
800	film bulk layer	3.62 ± 0.02	53.2 ± 0.1	75.9 ± 0.05	68 ± 6	192 ± 4
	interface layer	3.85 ± 0.05	51.5 ± 0.8	73.7 ± 2	295 ± 5	10 ± 2
900	film bulk layer	3.66 ± 0.03	52.2 ± 0.1	75.3 ± 0.05	86 ± 4	139 ± 2
	interface layer	3.92 ± 0.05	51.2 ± 0.9	73.5 ± 3	320 ± 4	20 ± 1
950	film bulk layer	3.80 ± 0.02	51.8 ± 0.1	74.8 ± 0.03	95 ± 6	114 ± 3
	interface layer	3.96 ± 0.05	51.0 ± 0.8	73.1 ± 2	336 ± 5	29 ± 2

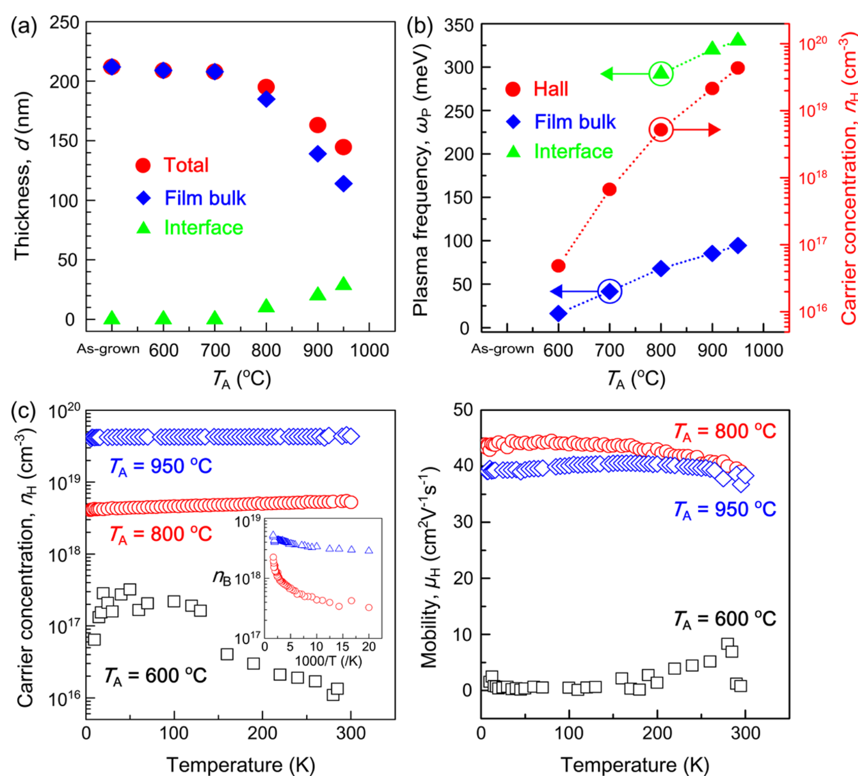

Figure 5. (a) Thickness (d) variation on the total, film bulk, and interface with increasing T_A (presented in Table 1). (b) Plots of plasma frequencies (ω_P) for the film bulk and interface layers and carrier concentration (n_H) as a function of T_A. (c) Temperature dependent n_H and mobility (μ_H) for the BZO films annealed at T_A = 600, 800, and 950 °C. The inset in (c) shows corrected film bulk carrier concentration (n_B) versus inverse temperature for the BZO films annealed at T_A = 800 and 950 °C.

Here, $\tilde{\omega}_{LPP,i}$ and $\tilde{\gamma}_{LPP,i}$ are the eigenfrequencies and broadening parameters of free carriers and lattice phonon modes (the LPP modes). The screened frequency of the lower (i = 1) and higher (i = 2) LPP modes are given by

$$\tilde{\omega}_{LPP,i} = \left\{ \frac{1}{2}\left[{\omega_{LO}}^2 + {\omega_p}^2 + (-1)^i \cdot \sqrt{({\omega_{LO}}^2 + {\omega_p}^2)^2 - 4{\omega_p}^2{\omega_{TO}}^2} \right] \right\}^{1/2} \quad (3)$$

The reflectance spectra of the as-grown and annealed samples at $T_A \leq 700$ °C were modeled taking a three-layer stratified medium as vacuum/film/substrate. In contrast, the samples annealed at $T_A \geq 800$ °C were modeled assuming a four-layer stratified medium by dividing the film into a bulk and an interface layer. The experimental data and simulation together with schematics of the sample layers are shown in Figure 4a. The factorized model was used for the simulation of the Al_2O_3 substrate, where the dielectric constants and phonon modes are used as input parameters. The effect of thermally nucleated NPs at the surface was accounted for by taking their incoherent optical response in the IR reflectance simulation. The extracted parameters are given in Table 1.

Figure 4b shows plots of the phonon energy of E_1(TO) and (LO) modes for the BZO films as a function of T_A. The result shows that both the E_1(TO) and (LO) bulk phonon energies gradually red-shifted to lower phonon energies with increasing T_A. As a consequence of the Be substitution in the host ZnO lattice, higher lattice vibration energies (phonon energies) were seen compared to that of undoped ZnO [see Figure 4a]. This is due to the smaller reduced mass and stronger bonding of Be−O compared to Zn−O in the WZ lattice. This corroborates the decrease of the lattice phonon energies attributed from the out-diffusion of Be from the BZO bulk during the annealing

process. The phonon energies of the interface layers for $T_A \geq$ 800 °C are also close to those of the undoped ZnO [$E_1(TO)$ = 50.8 meV and $E_1(LO)$ = 72.7 meV].[40] This implies a lower Be concentration at the interface compared to the bulk region.

As mentioned above, three additional impurity modes were observed at IM_1 = 82.6 meV, IM_2 = 98 meV, and IM_3 = 106 meV [Figure 4c]. No specific origin of these impurity modes has been reported to date. The second term in eq 1 describes the perturbation to host lattice phonon modes arising from the local potential of impurities. Hence, within this model, these modes could be attributed to local multiphonon modes associated with BeO segregation and intrinsic lattice defects.[41,42] The polarity splitting parameters (broadening constants) of these impurity modes increased (decreased) with T_A, suggesting an increase in local segregation of BeO and defect density within the annealed BZO films.

2.4. Temperature Dependent Carrier Concentration and the Double-Charge Layer Approximation. The IR reflectance simulation results are summarized in Table 1 and show that the thickness of the layers within the BZO films varies as a function of T_A. These results indicate that the total and bulk thicknesses significantly decrease when $T_A \geq$ 800 °C, while the interface layer thickness increases. This effect is shown in Figure 5a and could be due to thermally dissociated Zn−O bonds or an increase in density of textured grains. In our previous work, the effect of thermal treatment on the thickness variation in BZO films with different Be concentrations was investigated.[30] A high dissociation ratio in undoped ZnO films was observed as T_A above 800 °C, accompanied by a sudden decrase in the film thickness. Hence, the thickness reduction in the BZO films is mainly attributed to thermally induced lattice dissociation of the Zn−O bond during the thermal annealing process.

In order to account for the distribution of carriers within the films, the plasma frequency of each layer is plotted as a function of T_A in Figure 5b. A monotonic increase in the plasma frequency was observed in both layers with the increase of T_A. As the plasma frequency is proportional to the carrier concentration, a higher concentration was expected for higher T_A according to eq 5. This is consistent with the results of RT Hall effect measurements shown in Figure 5b. It is worthy of note that there is a large difference between the plasma frequency of the film bulk and interface layers for $T_A \geq$ 800 °C, and it reveals that the interface layer could be degenerate. Hence, variable temperature Hall effect measurements were performed in the range of 5−300 K for the BZO films annealed at T_A = 600, 800, and 950 °C, as illustrated in Figure 5c. The annealed BZO film (T_A = 600 °C) with no interface layer showed an anomalous temperature dependent carrier concentration with a mobility below 10 $cm^2V^{-1}s^{-1}$ across the entire temperature range. This unusual behavior could result from defect, grain boundary, or alloy scattering due to disorder in the phase-segregated alloy, observed in the XRD and AFM results. In contrast, the annealed BZO films at T_A = 800 and 950 °C showed temperature-independent Hall carrier concentration (n_H) and mobility (μ_H) values, supporting the existence of a degenerate layer at the BZO/substrate interface. By considering the classical freeze-out of carriers in the nondegenerate bulk region, the majority of carriers at low temperatures must come from the interface region. Hence, the sheet carrier density (n^s_{Int}) and mobility (μ_{Int}) in the interface layers were obtained by a linear extrapolation of the Hall data to 0 K. The interface carrier concentration, n_{Int}, was calculated by n^s_{Int}/d, where d is the thickness of the interface layer obtained from the IR reflectance simulations. The carrier concentration of the interface of the annealed BZO films at T_A = 800 and 950 °C were determined to be $n_{Int} = 7.54 \times 10^{19}$ and 2.16×10^{20} cm^{-3} and μ_{Int} = 43.80 and 39.05 $cm^2V^{-1}s^{-1}$, respectively. The interface conductivities ($\sigma_{Int} = n_{Int}e\mu_{Int}$) were calculated to be $\sigma_{Int} = 5.3 \times 10^2$ and 1.4×10^3 S·cm^{-1}, respectively. The carrier concentration and conductivity of double-layer films have been calculated by a parallel conduction model,[43]

$$n_B = \frac{(\mu_H n_H + \mu_{Int} n_{Int})^2}{{\mu_H}^2 n_H + {\mu_{Int}}^2 n_{Int}} \tag{4}$$

where n_B is the carrier concentration of the film bulk region. The corrected RT bulk carrier concentration of the films with T_A = 800 and 950 °C were found to be $n_B = 1.70 \times 10^{18}$ and 5.06×10^{18} cm^{-3}, respectively. By comparing the carrier concentrations and conductivities of the interfaces with those of the bulk, it is apparent that the interface values are much higher. Furthermore, the carrier concentrations in the interfaces (the bulk) are above (below) the Mott-transition level ($n \approx 6 \times 10^{18}$ cm^{-3}) of undoped ZnO.[44]

2.5. Discussion. The highly conductive layer, found at the BZO/Al_2O_3 interface, formed after high-temperature thermal treatment, $T_A \geq$ 800 °C, imposes degenerate semiconducting characteristics on all the BZO films. By using the physical quantities obtained from the analyses above, the density-of-states-averaged effective mass of conduction electrons, m^*_{av}, was calculated using,[38]

$$m^*_{av} = \frac{n_{Int} e^2}{{\omega_p}^2 \epsilon(0) \epsilon(\infty)} \tag{5}$$

where e is electronic charge, $\epsilon(0)$ is the permittivity of free space, and $\epsilon(\infty)$ is the high frequency dielectric constant. Values of $\epsilon(\infty)$ in the range of 3.85−3.96, obtained from the IR reflectance simulations, were used for the film interfaces with T_A = 800 and 950 °C. The $\epsilon(\infty)$ and m^*_{av} vary with carrier concentration in the interfaces. The m^*_{av} of the interface layers were determined to be $0.31m_0$ and $0.67m_0$ for carrier concentrations of $n_{Int} = 7.54 \times 10^{19}$ and 2.16×10^{20} cm^{-3}, respectively. This is reasonable as the Fermi level position increases with carrier concentration. Variation of the average effective mass with carrier concentration has been found previously in highly doped ZnO and doped $Mg_xZn_{1-x}O$ alloys.[45,46] Such a high carrier concentration at the interface, above the Mott-transition level, causes a strong band-filling effect (Burstein−Moss shift), along with the correlated band gap renormalization as a result of many-body effects.[47,48] Hence, the degenerate interface layer is important in deriving the physical properties of both BZO films and ZnO-based materials.

Here, we discuss possible atomic diffusion and phase transformation for the metastable BZO film with respect to T_A to explain the formation of the multilayer structure and degenerate interface layer.[35,49,50] The diffusion and segregation of Be were observed throughout the film with the resulting formation of secondary phase BeO NPs at the surface and grain boundaries. The phase separation phenomenon is caused when annealing temperatures exceed the solubility limit of Be into host ZnO as a phase miscibility gap, as observed in our previous study.[28] The driving force for such segregation processes is minimization of the total free energy (e.g., surface energy,

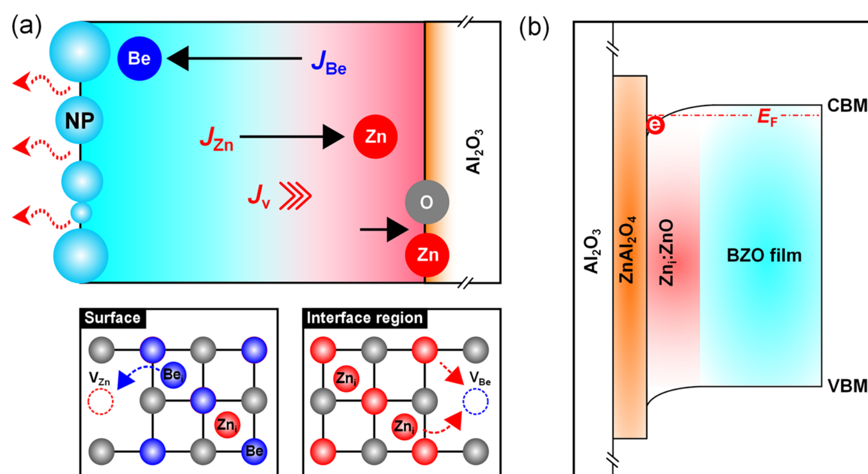

Figure 6. (a) Schematics of the atomic diffusion mechanism in the inner BZO film and the formation of surface BeO NPs and BZO/Al_2O_3 intermixing during solid-state reactions by thermal annealing. The Be flux (J_{Be}) is greater than the Zn flux (J_{Zn}) and thus the vacancy flux (J_V) toward the interface region. The bottom images represent the recrystallized surface associated with Be (blue sphere) diffusion, while Zn (red sphere) diffuses to the interface region of the film. (b) Schematic representation of the band lineup at the BZO film/Zn_i−ZnO/$ZnAl_2O_4$/Al_2O_3 heterostructure.

interfacial energy, elastic energy, etc.) of the metastable alloy system as Be atoms migrate from the bulk to the surface region.[28,51−53]

The high-temperature annealing ($T_A \geq 800$ °C) for the BZO films sufficiently leads to the outward diffusion of Be together with the dissociation of ZnO bonds. It is worth noting that the vapor pressure of Be is much lower than that of Zn, meaning that Be is less likely to evaporate from the surface. On this basis, at an early stage of the annealing processes, the depletion of Zn atoms at the surface and grain boundaries preferentially occurs as a result of evaporation, and in turn the enrichment of Be. This gives rise to a supersaturation condition for the nucleation of the secondary phase with a number of dilute atoms around the surface and even grain boundary regions, which are preferential pathways for atomic transport. The diffused/segregated Be atoms can be predominantly oxidized into the thermodynamically more stable BeO rather than ZnO as the free energy for the formation of the BeO [$E^F_{BeO} = E_{BeO} - (E_{Be} + E_O) = -5.839$ eV at 0 K] is much lower than that of ZnO [$E^F_{ZnO} = E_{ZnO} - (E_{Zn} + E_O) = -3.438$ eV at 0 K], obtained by density functional theory calculations (Table S1 in the Supporting Information). Therefore, the diffused/segregated Be atoms react with thermally diffused oxygen to form energetically favorable BeO at the surface and at grain boundaries. This enhances further nucleation and growth to minimize their free energies with T_A. This results in the distribution of the secondary phase BeO NPs at the surface and grain boundaries as presented in the STEM image. In other words, it is hard to recrystallize ZnO near Be-rich regions for thermally dissociated Zn atoms because Be acts as an effective oxygen trap to release the free energies. Furthermore, the nucleated/grown secondary phase BeO NPs placed at the pathways of mass transport could passivate the sublimation of residual Zn atoms from the film. This phenomenon, in conjunction with thermally induced thickness reduction, causes the observed excess of Zn interstitials in the annealed films.

Concurrently, the induced outward diffusion of Be atoms creates vacancies, e.g., V_{Be}, near the interface, resulting in a vacancy flux, $J_V = J_{Be} - J_{Zn}$, where J_{Be} and J_{Zn} are diffusion fluxes of Be and Zn.[33,54] This gives rise to the inward migration of Zn atoms toward the interface to minimize the chemical potential gradient.[55,56] As a result, a Zn concentration gradient from the surface toward the interface is observed from the *Z*-contrast STEM and EDS measurements (Figure 2a,b). In the high-temperature recrystallization processes, such inward diffusing Zn atoms effectively compensate for atomic vacancy sites, both V_{Zn} and V_{Be}. This defect compensation with high T_A corresponds to an improvement of the crystalline quality of the film and a notable decrease in the associated deep level emission of the isolated V_{Zn} and their clusters (observed in XRD and photoluminescence—Figures S1 and S5 in the Supporting Information). However, in the simultaneous occurrence of the atomic diffusion and following recrystallization, no significant correlation between the distribution of O and the cation density gradient was found in the high-temperature annealed film. This is seen in the almost constant EDS intensity of O throughout the film, and hence, diffusion proceeds predominantly by counter-diffusion of Be and Zn with a constant distribution of oxygen most likely.[35] Consequently, such cation counter-diffusion of Be and Zn (competition and repulsion) primarily and separately contributes to the formation of the Be-rich surface and Zn-rich interface in the high-temperature annealed alloy film. The diffusion of Zn and O (either in the form of ZnO or Zn and O ions) into Al_2O_3, as a unilateral atomic transfer, was also observed in the reaction interface, forming spinel $ZnAl_2O_4$ and Zn-deficient phase $Zn_xAl_yO_z$.[57]

On the basis of the above diffusion processes at high T_A, an accumulation of Zn is formed, which creates a Zn-rich ZnO (Zn_i−ZnO) interface region within the film. Several groups have reported that Zn_i acts as a source of donors due to its shallow defect states (≈31−37 meV) below the CBM, while V_O defects create deep level states in the band gap of ZnO.[5,58,59] In spite of many studies claiming that interstitial hydrogen behaves as a shallow donor in *n*-type ZnO, we assert that this is not the case in our samples. This is because the samples have been annealed at $T_A \geq 600$ °C, where hydrogen atoms rapidly out-diffuse from the sample.[5,60] Hence, we believe that the interface conductivity is primarily associated with the distribution of Zn_i. Due to the high accumulation of such shallow donor-like defects, the defect bands are expected to merge with the conduction band, leading to band gap renormalization and a

highly conductive interface layer in the high-temperature annealed alloy films as schematically illustrated in Figure 6b.[48] The Fermi level is located above the CBM as a result of downward band bending associated with the accumulation of electrons.[9] The band lineup presented in Figure 6b is an idealistic representation, as the effects of local Be composition and charged dislocations[12] in the Fermi energy have been disregarded and the bulk considered to be most likely ZnO. The Fermi level position for the highest conductive interface layer is calculated to be 266 meV above the CBM (see Figure S4 in the Supporting Information). The achieved conductivity of 1.4×10^3 S·cm^{-1} for the degenerate interface layer is close to the highest values achieved in Al/Ga doped ZnO films for similar carrier concentrations.[61,62] However, a simultaneous increase in the concentration of negatively charged compensating defects, especially V_{Zn}, should occur due to lowering of their formation energies as the Fermi level gets closer to the CNL in ZnO-based materials.[19,63] For the Fermi energies above this level, the formation of the *p*-type defects such as V_{Zn} becomes energetically favorable, based on the amphoteric defect model.[64,65] In recent studies,[62,66] to prevent such self-compensation, the suppression of formation of acceptor-like defects has been proposed by intentional doping to form dopant-defect complexes, e.g., Ga_{Zn}-V_{Zn}, maintaining high carrier concentration and mobility in heavily doped ZnO. In the cation counter-diffusion processes, sufficiently driven by high temperature annealing, the inward diffused Zn atoms within the isolated film region significantly reduce the negatively charged compensating defects during recrystallization, and subsequently, the new Zn arrivals become positively charged interstitials. This also leads to securing a high conductivity in the interface region of the annealed BZO film. The ratio of Be concentration to Zn and the reaction time will be other important parameters to control the accumulation of donor-like defects.[30] Controlling the distribution of defects through atomic counter-diffusion processes in $Be_xZn_{1-x}O$ alloys as well as other oxides will be essential and promising in future applications such as nanoscale transparent conductive transistors and in the fabrication of core–shell alloy nanostructures such as quantum wells in nanowires and hollow nanotubes/nanoparticles.

3. CONCLUSIONS

We have demonstrated the effect of thermal treatment on multiphase crystalline BZO films. Thermal treatment (T_A = 600–950 °C) leads to recrystallization of the metastable alloy along with atomic redistribution and strain relaxation. Thermally induced lattice dissociation and out-diffusion of Be results in a pronounced microstructural segregation and precipitation of donor-like defects such as Zn_i. These observations are accompanied by a decrease in the band gap energy and lattice phonon energy of the BZO films. For $T_A \geq$ 800 °C, highly conductive layers with thicknesses in the range of 10–29 nm are generated at the near-interface region of the BZO film/Al_2O_3 substrate. The plasma frequency of the interfaces range from 295 to 336 meV, corresponding to carrier concentrations from $n_{Int} = 7.54 \times 10^{19}$ to 2.16×10^{20} cm^{-3}. The interface region with such high carrier concentrations show degenerate characteristics with high conductivities in the range of $\sigma_{Int} = 5.3 \times 10^2$–$1.4 \times 10^3$ S·cm^{-1}. IR reflectance simulations and a parallel conduction model enable determination of the average effective mass of the conduction electrons in the interface layers which ranges from $0.31m_0$ to $0.67m_0$. Hence, the degenerate interface layers are found to significantly influence the electronic and optical properties of the BZO films. Such nanoscale interface conductivities achieved in the high-temperature annealed BZO films are comparable to the highest values obtained in doped ZnO. A cation counter-diffusion mechanism is proposed to interpret the high accumulation of donor-like defects and the subsequent formation of the degenerate interface layer within the annealed alloy films. This study extensively contributes to the understanding for the thermodynamics of defect engineering of metastable $Be_xZn_{1-x}O$ alloys, and opens up a new era for wide band gap oxide-based alloy applications.

4. EXPERIMENTAL SECTION

The BZO ternary film was grown on an $Al_2O_3(0001)$ substrate at 500 °C, in a partial pressure (P_{O2}) of 2×10^{-3} mbar (base pressure: 1.6×10^{-8} mbar) by radio frequency (RF) magnetron co-sputtering. The as-grown film was thermally treated at various temperatures between 600 and 950 °C for 60 min with N_2 gas flowing. All annealing temperatures were set up with a ramping rate of 20 °C/min.

Structural changes for the as-grown and thermally annealed films were characterized by high-resolution X-ray diffraction using a Panalytical X'Pert Pro MRD equipped with an incident beam hybrid monochromator giving pure Cu $K_{\alpha 1}$ radiation (HRXRD: λ = 1.5406 Å). Surface morphology was studied with tapping-mode AFM measurements. A PerkinElmer Lambda 25 UV/vis spectrometer was used to determine the optical band gap energy of the as-grown and annealed BZO films. XPS measurements were performed in ultrahigh vacuum (UHV; base pressure = 3×10^{-11} mbar) using an Omicron SPHERA hemispherical analyzer and a monochromatic Al K_α X-ray source ($h\nu$ = 1486.6 eV). Photoelectrons emitted from the film surfaces were collected at normal emission. During the XPS measurements, the surface charging effects were compensated using a low energy electron flood gun (Omicron CN10). The overall energy resolution was 0.47 eV, and the BE scale was calibrated using the adventitious C 1s peak (BE = 284.5 eV). The transmission function of the analyzer was calibrated using Ag, Au, and Cu foils. The XPS spectra were fitted using a Shirley background and Voigt function. Also, compositional ratios for each element (Zn, O, Be, and C) in the ternary films were determined, correcting for the electron mean free path and using Scofield cross sections.[67] Far- and mid-IR reflectance measurements at an incident angle of 11° relative to the film surface normal were recorded using a Bruker Vertex 70v Fourier-transform infrared (FTIR) spectrometer. Because of the optical anisotropy of the polar crystal, *s*-polarized far-IR and mid-IR reflectance spectra for the films were obtained by polyethylene (50–600 cm^{-1}) and ZnSe (460–8000 cm^{-1}) polarizers. The reflectance spectra were simulated utilizing a stratified medium consisting of 3 layers (4 layers) for as-grown and annealed, $T_A \leq$ 700 °C (annealed, T_A = 800–950 °C), samples with coherent interference. The electrical properties of the films were characterized by performing variable temperature (5–300 K) Hall-effect measurements in the Van der Pauw configuration. Indium solder was used to make ohmic contacts to all of the etched corners of the 5 × 5 mm^2 samples. Field emission transmission electron microscopy (FETEM, a Tecnai G^2 F30 S-Twin), equipped with energy dispersive spectroscopy (EDX, EDAX Genesis), was used with an acceleration voltage of 300 kV to characterize the microstructural properties, and elemental profiling of the annealed BZO sample at T_A = 950 °C was performed. In order to examine the defect distribution in the BZO films as a function of T_A, variable temperature (T = 12–300 K) photoluminescence measurements were carried out using a He–Cd laser (λ = 325 nm). An integrated long-pass optical filter with a cutoff wavelength of 420 nm was used to increase the dynamic range of deep-level-associated emissions in the samples.

■ ASSOCIATED CONTENT

Supporting Information

High-resolution and powder X-ray diffractions of the as-grown and annealed BZO films with T_A; tapping-mode atomic force microscopy images of the BZO films; the calculation of the Fermi-level position of the highly conductive interface layer in the annealed BZO film (T_A = 950 °C); the photoluminescence spectra of the as-grown and annealed films; the calculations of formation energies of ZnO and BeO. This material is available free of charge via the Internet at http://pubs.acs.org/.

■ AUTHOR INFORMATION

Corresponding Author

*E-mail: c.f.mcconville@warwick.ac.uk.

Notes

The authors declare no competing financial interest.

■ ACKNOWLEDGMENTS

The authors acknowledge technical support from Prof. G. Balakrishnan and R. I. Johnston in the Department of Physics at the University of Warwick, UK. The authors are grateful for valuable discussions from Dr. D. Holland and Dr. D. Walker at the University of Warwick. Access to equipment used in this study was provided through the Science City Research Alliance (SCRA) with capital equipment funding from Advantage West Midlands (AWM) and the European Research and Development Fund (ERDF). D.-S. Park also acknowledges funding from the University of Warwick for the award of a Chancellor's Scholarship.

■ REFERENCES

(1) Tsukazaki, A.; Akasaka, S.; Nakahara, K.; Ohno, Y.; Ohno, H.; Maryenko, D.; Ohtomo, A.; Kawasaki, M. Observation of the Fractional Quantum Hall Effect in an Oxide. *Nat. Mater.* **2010**, *9*, 889−893.

(2) Nakagawa, N.; Hwang, H. Y.; Muller, D. A. Why Some Interfaces Cannot Be Sharp. *Nat. Mater.* **2006**, *5*, 204−209.

(3) Ohtomo, A.; Hwang, H. Y. A High-Mobility Electron Gas at the $LaAlO_3/SrTiO_3$ Heterointerface. *Nature* **2004**, *427*, 423−426.

(4) Tsukazaki, A.; Ohtomo, A.; Kita, T.; Ohno, Y.; Ohno, H.; Kawasaki, M. Quantum Hall Effect in Polar Oxide Heterostructures. *Science* **2007**, *315*, 1388−1391.

(5) Janotti, A.; de Walle, C. G. V. Fundamentals of Zinc Oxide as a Semiconductor. *Rep. Prog. Phys.* **2009**, *72*, 126501−126529.

(6) Ohtomo, A.; Kawasaki, M.; Koida, T.; Masubuchi, K.; Koinuma, H.; Sakurai, Y.; Yoshida, Y.; Yasuda, T.; Segawa, Y. $Mg_xZn_{1-x}O$ as a II−VI Widegap Semiconductor Alloy. *Appl. Phys. Lett.* **1998**, *72*, 2466−2468.

(7) Ryu, Y. R.; Lee, T. S.; Lubguban, J. A.; Corman, A. B.; White, H. W.; Leem, J. H.; Han, M. S.; Park, Y. S.; Youn, C. J.; Kim, W. J. Wide-Band Gap Oxide Alloy: BeZnO. *Appl. Phys. Lett.* **2006**, *88*, 052103−052104.

(8) Choi, W. S.; Chisholm, M. F.; Singh, D. J.; Choi, T.; Jellison, G. E.; Lee, H. N. Wide Bandgap Tunability in Complex Transition Metal Oxides by Site-Specific Substitution. *Nat. Commun.* **2012**, *3*, 689−694.

(9) King, P. D. C.; Veal, T. D.; Payne, D. J.; Bourlange, A.; Egdell, R. G.; McConville, C. F. Surface Electron Accumulation and the Charge Neutrality Level in In_2O_3. *Phys. Rev. Lett.* **2008**, *101*, 116808−116811.

(10) King, P. D. C.; Veal, T. D.; Schleife, A.; Zúñiga-Pérez, J.; Martel, B.; Jefferson, P. H.; Fuchs, F.; Muñoz Sanjosé, V.; Bechstedt, F.; McConville, C. F. Valence-Band Electronic Structure of CdO, ZnO, and MgO from X-Ray Photoemission Spectroscopy and Quasi-Particle-Corrected Density-Functional Theory Calculations. *Phys. Rev. B* **2009**, *79*, 205205−205210.

(11) Allen, M. W.; Zemlyanov, D. Y.; Waterhouse, G. I. N.; Metson, J. B.; Veal, T. D.; McConville, C. F.; Durbin, S. M. Polarity Effects in the X-Ray Photoemission of ZnO and other Wurtzite Semiconductors. *Appl. Phys. Lett.* **2011**, *98*, 101906−101908.

(12) Vasheghani Farahani, S. K.; Veal, T. D.; Sanchez, A. M.; Bierwagen, O.; White, M. E.; Gorfman, S.; Thomas, P. A.; Speck, J. S.; McConville, C. F. Influence of Charged-Dislocation Density Variations on Carrier Mobility in Heteroepitaxial Semiconductors: The Case of SnO_2 on Sapphire. *Phys. Rev. B* **2012**, *86*, 245315−245321.

(13) Service, R. F. Will UV Lasers Beat the Blues? *Science* **1997**, *276*, 895.

(14) Janotti, A.; Van de Walle, C. G. Native Point Defects in ZnO. *Phys. Rev. B* **2007**, *76*, 165202−165223.

(15) Long, H.; Fang, G.; Li, S.; Mo, X.; Wang, H.; Huang, H.; Jiang, Q.; Wang, J.; Zhao, X. A ZnO/ZnMgO Multiple-Quantum-Well Ultraviolet Random Laser Diode. *IEEE Electron Device Lett.* **2011**, *32*, 54−56.

(16) Chu, S.; Wang, G.; Zhou, W.; Lin, Y.; Chernyak, L.; Zhao, J.; Kong, J.; Li, L.; Ren, J.; Liu, J. Electrically Pumped Waveguide Lasing from ZnO Nanowires. *Nat. Nanotechnol.* **2011**, *6*, 506−510.

(17) Heo, Y. W.; Kwon, Y. W.; Li, Y.; Pearton, S. J.; Norton, D. P. P-Type Behavior in Phosphorus-Doped (Zn,Mg)O Device Structures. *Appl. Phys. Lett.* **2004**, *84*, 3474−3476.

(18) Nakahara, K.; Akasaka, S.; Yuji, H.; Tamura, K.; Fujii, T.; Nishimoto, Y.; Takamizu, D.; Sasaki, A.; Tanabe, T.; Takasu, H.; Amaike, H.; Onuma, T.; Chichibu, S. F.; Tsukazaki, A.; Ohtomo, A.; Kawasaki, M. Nitrogen Doped $Mg_xZn_{1-x}O$/ZnO Single Heterostructure Ultraviolet Light-Emitting Diodes on ZnO Substrates. *Appl. Phys. Lett.* **2010**, *97*, 013501−013503.

(19) Schleife, A.; Fuchs, F.; Rödl, C.; Furthmüller, J.; Bechstedt, F. Branch-Point Energies and Band Discontinuities of III-Nitrides and III-/II-Oxides from Quasiparticle Band-Structure Calculations. *Appl. Phys. Lett.* **2009**, *94*, 012104−012106.

(20) Van de Walle, C. G.; Neugebauer, J. Universal Alignment of Hydrogen Levels in Semiconductors, Insulators, and Solutions. *Nature (London)* **2003**, *423*, 626−628.

(21) Mosbacker, H. L.; Zgrabik, C.; Hetzer, M. J.; Swain, A.; Look, D. C.; Cantwell, G.; Zhang, J.; Song, J. J.; Brillson, L. J. Thermally Driven Defect Formation and Blocking Layers at Metal-ZnO Interfaces. *Appl. Phys. Lett.* **2007**, *91*, 072102−072104.

(22) Ryu, Y. R.; Lee, T. S.; Lubguban, J. A.; White, H. W.; Kim, B. J.; Park, Y. S.; Youn, C. J. Next Generation of Oxide Photonic Devices: ZnO-Based Ultraviolet Light Emitting Diodes. *Appl. Phys. Lett.* **2006**, *88*, 241108−241110.

(23) Venkatachalapathy, V.; Galeckas, A.; Trunk, M.; Zhang, T.; Azarov, A.; Kuznetsov, A. Y. Understanding Phase Separation in ZnCdO by a Combination of Structural and Optical Analysis. *Phys. Rev. B* **2011**, *83*, 125315−125325.

(24) Park, D.-S.; Mudd, J. J.; Walker, M.; Seghier, D.; Krupski, A.; Saniee, N. F.; Choi, C.-J.; Youn, C. J.; McMitchell, S. R. C.; McConville, C. F. Pinning Effect on the Band Gap Modulation of Crystalline $Be_xZn_{1-x}O$ Alloy Films grown on $Al_2O_3(0001)$. *CrystEngComm* **2014**, *16*, 2136−2143.

(25) Gan, C. K.; Fan, X. F.; Kuo, J.-L. Composition-Temperature Phase Diagram of $Be_xZn_{1-x}O$ from First Principles. *Comput. Mater. Sci.* **2010**, *49*, S29−S31.

(26) Liu, W.-R.; Lin, B. H.; Yang, S.; Kuo, C. C.; Li, Y.-H.; Hsu, C.-H.; Hsieh, W. F.; Lee, W. C.; Hong, M.; Kwo, J. The Influence of Dislocations on Optical and Electrical Properties of Epitaxial ZnO on Si (111) using a γ-Al_2O_3 Buffer Layer. *CrystEngComm* **2012**, *14*, 1665−1671.

(27) Kim, I. W.; Lee, K. M. Temperature Dependence of Microstructure and Strain Evolution in Strained ZnO Films on Al_2O_3 (0001). *Nanotechnology* **2008**, *19*, 355709−355715.

(28) Park, D.-S.; Krupski, A.; Sanchez, A. M.; Choi, C.-J.; Yi, M.-S.; Lee, H.-H.; McMitchell, S. R. C.; McConville, C. F. Optimal Growth and Thermal Stability of Crystalline $Be_{0.25}Zn_{0.75}O$ Alloy Films on $Al_2O_3(0001)$. *Appl. Phys. Lett.* **2014**, *104*, 141902−141906.

(29) Denton, A. R.; Ashcroft, N. W. Vegard's Law. *Phys. Rev. A* **1991**, *43*, 3161−3164.
(30) Park, D.-S.; Walker, M.; Vasheghani Farahani, S. K.; Wang, H.; Mudd, J. J.; Choi, C.-J.; McConville, C. F., submitted for publication.
(31) Yao, T.; Hong, S.-K. *Oxide and Nitride Semiconductors: Processing, Properties, and Applications*; Springer: Berlin, 2010; Chapter 1, pp 4−5.
(32) Wang, Y.; Liao, Q.; Lei, H.; Zhang, X.; Ai, X.; Zhang, J.; Wu, K. Interfacial Reaction Growth: Morphology, Composition, and Structure Controls in Preparation of Crystalline $Zn_xAl_yO_z$ Nanonets. *Adv. Mater.* **2006**, *18*, 943−947.
(33) Fan, X. F.; Zhu, Z.; Ong, Y.-S.; Lu, Y. M.; Shen, Z. X.; Kuo, J.-L. A Direct First Principles Study on the Structure and Electronic Properties of $Be_xZn_{1-x}O$. *Appl. Phys. Lett.* **2007**, *91*, 121121−121123.
(34) Pennycook, S. Z-Contrast Transmission Electron Microscopy:Direct Atomic Imaging of Materials. *Annu. Rev. Mater. Sci.* **1992**, *22*, 171−195.
(35) Fan, H. J.; Knez, M.; Scholz, R.; Nielsch, K.; Pippel, E.; Hesse, D.; Zacharias, M.; Gosele, U. Monocrystalline Spinel Nanotube Fabrication Based on the Kirkendall Effect. *Nat. Mater.* **2006**, *5*, 627−631.
(36) Damen, T. C.; Porto, S. P. S.; Tell, B. Raman Effect in Zinc Oxide. *Phys. Rev.* **1966**, *142*, 570−574.
(37) Calleja, J. M.; Cardona, M. Resonant Raman Scattering in ZnO. *Phys. Rev. B* **1977**, *16*, 3753−3761.
(38) Kasic, A.; Schubert, M.; Einfeldt, S.; Hommel, D.; Tiwald, T. E. Free-Carrier and Phonon Properties of *n*- and *p*-Type Hexagonal GaN Films Measured by Infrared Ellipsometry. *Phys. Rev. B* **2000**, *62*, 7365−7377.
(39) Ashkenov, N.; Mbenkum, B. N.; Bundesmann, C.; Riede, V.; Lorenz, M.; Spemann, D.; Kaidashev, E. M.; Kasic, A.; Schubert, M.; Grundmann, M.; Wagner, G.; Neumann, H.; Darakchieva, V.; Arwin, H.; Monemar, B. Infrared Dielectric Functions and Phonon mModes of High-Quality ZnO Films. *J. Appl. Phys.* **2003**, *93*, 126−133.
(40) Ellmer, K.; Klein, A.; Rech, B. *Transparent Conductive Zinc Oxide: Basics and Applications in Thin Film Solar Cells*; Springer: Berlin, 2008; Chapter 3, pp 92−102.
(41) Cuscó, R.; Alarcón-Lladó, E.; Ibáñez, J.; Artús, L.; Jiménez, J.; Wang, B.; Callahan, M. J. Temperature Dependence of Raman Scattering in ZnO. *Phys. Rev. B* **2007**, *75*, 165202−165212.
(42) Senthilkumar, K.; Tokunaga, M.; Okamoto, H.; Senthilkumar, O.; Fujita, Y. Hydrogen Related Defect Complexes in ZnO Nanoparticles. *Appl. Phys. Lett.* **2010**, *97*, 091907−091909.
(43) Petritz, R. L. Theory of an Experiment for Measuring the Mobility and Density of Carriers in the Space-Charge Region of a Semiconductor Surface. *Phys. Rev.* **1958**, *110*, 1254−1262.
(44) Tampo, H.; Yamada, A.; Fons, P.; Shibata, H.; Matsubara, K.; Iwata, K.; Niki, S.; Nakahara, K.; Takasu, H. Degenerate Layers in Epitaxial ZnO Films Grown on Sapphire Substrates. *Appl. Phys. Lett.* **2004**, *84*, 4412−4414.
(45) Fujiwara, H.; Kondo, M. Effects of Carrier Concentration on the Dielectric Function of ZnO:Ga and In_2O_3:Sn studied by Spectroscopic Ellipsometry: Analysis of Free-Carrier and Band-Edge Absorption. *Phys. Rev. B* **2005**, *71*, 075109−075118.
(46) Lu, J. G.; Fujita, S.; Kawaharamura, T.; Nishinaka, H.; Kamada, Y.; Ohshima, T. Carrier Concentration Induced Band-Gap Shift in Al-Doped $Zn_{1-x}Mg_xO$ Thin Films. *Appl. Phys. Lett.* **2006**, *89*, 262107−262109.
(47) Roth, A. P.; Webb, J. B.; Williams, D. F. Band-Gap Narrowing in Heavily Defect-Doped ZnO. *Phys. Rev. B* **1982**, *25*, 7836−7839.
(48) Sernelius, B. E.; Berggren, K.-F.; Jin, Z.-C.; Hamberg, I.; Granqvist, C. G. Band-Gap Tailoring of ZnO by Means of Heavy Al Doping. *Phys. Rev. B* **1988**, *37*, 10244−10248.
(49) Porter, D. A.; Easterling, K. E.; Sherif, M. Y. *Phase Transformations in Metals and Alloys*, 3rd ed.; CRC Press: Boca Raton, FL, 2008; Chapter 2, pp 65−107.
(50) Williams, F. L.; Nason, D. Binary Alloy Surface Compositions from Bulk Alloy Thermodynamic Data. *Surf. Sci.* **1974**, *45*, 377−408.
(51) Es-Souni, M. Computer Simulation of Segregation Kinetics in Ternary Alloys. *Scr. Metall. Mater.* **1989**, *23*, 919−924.
(52) Bogusławski, P.; Bernholc, J. Surface Segregation of Ge at SiGe(100) by Concerted Exchange Pathway. *Phys. Rev. Lett.* **2002**, *88*, 166101−166104.
(53) Stamenkovic, V. R.; Mun, B. S.; Mayrhofer, K. J. J.; Ross, P. N.; Markovic, N. M. Effect of Surface Composition on Electronic Structure, Stability, and Electrocatalytic Properties of Pt-Transition Metal Alloys: Pt-Skin versus Pt-Skeleton Surfaces. *J. Am. Chem. Soc.* **2006**, *128*, 8813−8819.
(54) Tu, K. N.; Gösele, U. Hollow Nanostructures Based on the Kirkendall Effect: Design and Stability Considerations. *Appl. Phys. Lett.* **2005**, *86*, 093111−093113.
(55) Darken, L. S. Diffusion of Carbon in Austenite with a Discontinuity in Composition. *Trans. AIME* **1949**, *180*, 430−438.
(56) Baird, R. J.; Potter, T. J.; Kothiyal, G. P.; Bhattacharya, P. K. Indium Diffusion in the Chemical Potential Gradient at an $In_{0.53}Ga_{0.47}As/In_{0.52}Al_{0.48}As$ Interface. *Appl. Phys. Lett.* **1988**, *52*, 2055−2057.
(57) Fan, H. J.; Yang, Y.; Zacharias, M. ZnO-Based Ternary Compound Nanotubes and Nanowires. *J. Mater. Chem.* **2009**, *19*, 885−900.
(58) Look, D. C.; Hemsky, J. W.; Sizelove, J. R. Residual Native Shallow Donor in ZnO. *Phys. Rev. Lett.* **1999**, *82*, 2552−2555.
(59) Sann, J.; Stehr, J.; Hofstaetter, A.; Hofmann, D. M.; Neumann, A.; Lerch, M.; Haboeck, U.; Hoffmann, A.; Thomsen, C. Zn Interstitial Related Donors in Ammonia-Treated ZnO Powders. *Phys. Rev. B* **2007**, *76*, 195203−195208.
(60) Nickel, N. H. Hydrogen Migration in Single Crystal and Polycrystalline Zinc Oxide. *Phys. Rev. B* **2006**, *73*, 195204−195212.
(61) Kim, K.-K.; Niki, S.; Oh, J.-Y.; Song, J.-O.; Seong, T.-Y.; Park, S.-J.; Fujita, S.; Kim, S.-W. High Electron Concentration and Mobility in Al-Doped *n*-ZnO Epilayer Achieved via Dopant Activation Using Rapid-Thermal Annealing. *J. Appl. Phys.* **2005**, *97*, 066103−066105.
(62) Look, D. C.; Leedy, K. D.; Vines, L.; Svensson, B. G.; Zubiaga, A.; Tuomisto, F.; Doutt, D. R.; Brillson, L. J. Self-Compensation in Semiconductors: The Zn Vacancy in Ga-Doped ZnO. *Phys. Rev. B* **2011**, *84*, 115202−115207.
(63) Demchenko, D. O.; Earles, B.; Liu, H. Y.; Avrutin, V.; Izyumskaya, N.; Özgür, U.; Morkoç, H. Impurity Complexes and Conductivity of Ga-Doped ZnO. *Phys. Rev. B* **2011**, *84*, 075201−075201.
(64) Walukiewicz, W. Amphoteric Native Defects in Semiconductors. *Appl. Phys. Lett.* **1989**, *54*, 2094−2096.
(65) Burbano, M.; Scanlon, D. O.; Watson, G. W. Sources of Conductivity and Doping Limits in CdO from Hybrid Density Functional Theory. *J. Am. Chem. Soc.* **2011**, *133*, 15065−15072.
(66) Ke, Y.; Lany, S.; Berry, J. J.; Perkins, J. D.; Parilla, P. A.; Zakutayev, A.; Ohno, T.; O'Hayre, R.; Ginley, D. S. Enhanced Electron Mobility Due to Dopant-Defect Pairing in Conductive ZnMgO. *Adv. Funct. Mater.* **2014**, *24*, 2875−2882.
(67) Scofield, J. Hartree-Slater Subshell Photoionization Cross-Sections at 1254 and 1487 eV. *J. Electron Spectrosc. Relat. Phenom.* **1976**, *8*, 129−137.